

1 **Revision 3**

2 **X-ray spectroscopy study of the chemical state of “invisible” Au in synthetic minerals in**  
3 **the Fe-As-S system**

4

5 Alexander L. Trigub<sup>2,1,8</sup>, Boris R. Tagirov<sup>1\*</sup>, Kristina O. Kvashnina<sup>3,9</sup>, Dmitriy A. Chareev<sup>4,1,7</sup>,  
6 Maximilian S. Nickolsky<sup>1</sup>, Andrey A. Shiryaev<sup>5,1</sup>, Nina N. Baranova<sup>6</sup>, Elena V. Kovalchuk<sup>1</sup> and  
7 Andrey V. Mokhov<sup>1</sup>

8

9

10

11 <sup>1</sup> Institute of Geology of Ore Deposits (IGEM RAS), 35, Staromonetnyi per., 119017 Moscow,  
12 Russia

13 <sup>2</sup> National Research Centre ‘Kurchatov Institute’, 1 Akademika Kurchatova Sq., 123182  
14 Moscow, Russia

15 <sup>3</sup> ESRF – The European Synchrotron, CS40220, 38043 Grenoble Cedex 9, France

16 <sup>4</sup> Institute of Experimental Mineralogy (IEM RAS), 142432 Chernogolovka, Moscow Region,  
17 Russia

18 <sup>5</sup> Institute of Physical Chemistry and Electrochemistry (IPCE RAS), 31 korp. 4, Leninsky  
19 Prospect, 119071 Moscow, Russia

20 <sup>6</sup> Vernadsky Institute of Geochemistry and Analytical Chemistry (GEOKHI RAS), 19, Kosygina  
21 str., 19991 Moscow, Russia

22 <sup>7</sup> Institute of Physics and Technology, Ural Federal University, Mira st., 19, 620002  
23 Ekaterinburg, Russia

24 <sup>8</sup> Physico-Technical Institute of UB RAS, Kirova st. 132, 426000 Izhevsk, Russia

25 <sup>9</sup> Helmholtz-Zentrum Dresden-Rossendorf (HZDR), Institute of Resource Ecology, P.O. Box  
26 510119, 01314, Dresden, Germany

27

28 \* corresponding author, E-mail: [borisl1@yandex.ru](mailto:borisl1@yandex.ru)

29 **Running title:** Trigub et al.: “Invisible” gold in sulfides

30 **Keywords:** invisible gold, pyrite, arsenopyrite, löllingite, synthetic minerals, X-ray absorption  
31 spectroscopy, atomic charges

32

33

### Abstract

34 Minerals of the Fe-As-S system are the main components of Au ores in many  
35 hydrothermal deposits, including Carlin-type Au deposits, volcanogenic massive sulfide  
36 deposits, epithermal, mesothermal, sedimentary-hosted systems, and Archean Au lodes. The  
37 “invisible” (or refractory) form of Au is present in all types of hydrothermal ores and often  
38 predominates. Knowledge of the chemical state of “invisible” Au (local atomic  
39 environment/structural position, electronic structure, and oxidation state) is crucial for  
40 understanding the conditions of ore formation and necessary for the physical-chemical modeling  
41 of hydrothermal Au mineralization. In addition, it will help to improve the technologies of ore  
42 processing and Au extraction. Here we report an investigation of the chemical state of “invisible”  
43 Au in synthetic analogues of natural minerals (As-free pyrite FeS<sub>2</sub>, arsenopyrite FeAsS, and  
44 löllingite FeAs<sub>2</sub>). The compounds were synthesized by means of hydrothermal (pyrite) and salt  
45 flux techniques (in each case) and studied by X-ray absorption fine structure (XAFS)  
46 spectroscopy in a high energy resolution fluorescence detection (HERFD) mode in combination  
47 with first-principles quantum chemical calculations. The content of “invisible” Au in the  
48 synthesized löllingite (800±300 ppm) was much higher than that in arsenopyrite (23±14 ppm).  
49 The lowest Au content was observed in zonal pyrite crystals synthesized in a salt flux. High  
50 “invisible” Au contents were observed in hydrothermal pyrite (40-90 ppm), which implies that  
51 this mineral can efficiently scavenge Au even in As-free systems. The Au content of the  
52 hydrothermal pyrite is independent of sulfur fugacity and probably corresponds to the maximum  
53 Au solubility at the experimental *P/T* parameters (450 °C, 1 kbar). It is shown that Au replaces  
54 Fe in the structures of löllingite, arsenopyrite, and hydrothermal pyrite. The Au-ligand distance  
55 increases by 0.14 Å (pyrite), 0.16 Å (löllingite), and 0.23 Å (As), 0.13 Å (S) (arsenopyrite)  
56 relative to the Fe-ligand distance in pure compounds. Distortions of the atomic structures are  
57 localized around Au atoms and disappear at  $R > \sim 4$  Å. Chemically bound Au occurs only in

58 hydrothermal pyrite, whereas pyrite synthesized without hydrothermal fluid contains only Au<sup>0</sup>.  
59 The heating (metamorphism) of hydrothermal pyrite results in the decomposition of chemically  
60 bound Au and formation of Au<sup>0</sup> nuggets, which coarsen with increasing temperature. Depending  
61 on the chemical composition of the host mineral, Au can play a role of either a cation or an  
62 anion: the Bader atomic partial charge of Au decreases in the order pyrite (+0.4 e) > arsenopyrite  
63 (0) > löllingite (-0.4 e). Our results suggest that other noble metals (platinum group elements,  
64 Ag) can form a chemically bound refractory admixture in base metal sulfides/chalcogenides. The  
65 content of chemically bound noble metals can vary depending on the composition of the host  
66 mineral and ore history.  
67

68

## Introduction

69 Minerals of the Fe-As-S system (pyrite FeS<sub>2</sub>, arsenopyrite FeAsS, and löllingite FeAs<sub>2</sub>)  
70 are ubiquitous in sulfide ores in many geologic environments and Au-bearing ore deposits,  
71 including Carlin-type Au deposits (for example, Palenik et al., 2004, and reference therein),  
72 volcanogenic massive sulfide (VMS) deposits (e.g. Mercier–Langevin et al., 2011; Vikentyev,  
73 2015a), mesothermal (Genkin et al., 1998), epithermal (e.g. Cook et al., 2009), sedimentary-  
74 hosted systems (Large et al., 2007), and Archean Au lodes (Goldfarb et al., 2005). These  
75 occurrences are an important source of Au, and many of them belong to world-class gold  
76 deposits (>100 t Au, c.f., Genkin et al., 1998; Mercier–Langevin et al., 2011). In these ores Au  
77 exists (i) as discrete minerals – compounds with chalcogens (S, Se, Te), semimetals (As, Sb, Bi),  
78 or intermetallic compounds with Cu, Ag, Hg, etc., and (ii) in an “invisible” (or refractory) state.  
79 “Invisible” Au includes nanoscale particles and Au solid solutions. Neither form can be  
80 identified by conventional optical or scanning electron microscopy. Visible nuggets of Au and  
81 Au-alloys can be extracted from the ore using, for example, cyanide leaching, whereas  
82 “invisible” Au cannot be extracted by conventional ore processing methods. In many deposits  
83 the proportion of “invisible” Au can be very high. For example, it reaches 85% at the Uchaly  
84 VMS deposit in the South Urals, Russia. The estimated total loss of Au from all VMS deposits of  
85 the South Urals region is 10-15 t per year (Vikentyev, 2015a).

86 In hydrothermal ores, pyrite often shows the maximal concentrations of “invisible” Au.  
87 In many cases, there is a positive correlation between Au and As in pyrite (e.g., Reich et al.,  
88 2005; Deditius et al., 2014), although deposits with Au-rich and As-poor pyrite are also known.  
89 For example, colloform pyrite bands and veinlets in the large Agua Rica Cu (Mo–Au) deposit  
90 (Argentina) are As-poor (<30 ppm) but contain up to 6.7 ppm Au (Franchini et al., 2015). A  
91 number of studies of Au-bearing deposits of the Urals (Russia), including VMS deposits  
92 (Vikentyev, 2015a, 2015b), Novogodnee-Monto Fe-Au-skarn deposit (Ivanova et al., 2015), and

93 Svetlinsk Au-Te deposit (Vikent'eva and Bortnikov, 2015), did not reveal any significant  
94 correlation between Au and As in pyrite. Hence, depending on the deposit type and ore  
95 formation conditions, both As-rich and As-poor pyrites can bear economic Au content, although  
96 the highest Au contents were documented in arsenian pyrites.

97       The understanding of the chemical state of “invisible” Au in sulfide ores is necessary for  
98 the physical-chemical modeling of hydrothermal Au mineralization and has important  
99 implications for the mineral processing industry. The chemical state of “invisible” Au, including  
100 its local atomic environment, position in the host mineral structure in the case of solid solution,  
101 and valence state can be reliably determined only by spectroscopic methods. Previously, Au-  
102 bearing sulfides were studied by X-ray photoelectron (XPS, see Widler and Seward, 2002 and  
103 reference therein; Laptev and Rozov, 2006), Mössbauer (Cardile et al., 1993; Genkin et al.,  
104 1998; Kozerenko et al., 2001), and X-ray absorption near edge structure (XANES) spectroscopy  
105 (Simon et al., 1999; Cabri et al., 2000). Our study aims at determining the chemical state of  
106 “invisible” Au in pyrite, arsenopyrite, and löllingite (FeAs<sub>2</sub>) by X-ray absorption spectroscopy  
107 (XAS) in a high energy resolution fluorescence detection mode (HERFD), with emphasis on Au  
108 solid solution. To estimate the conditions favoring formation of this form of “invisible” Au, we  
109 synthesized Au-bearing chalcogenides using different methods (hydrothermal and salt flux) at  
110 contrasting  $T/f(S_2)$  conditions, characterized the amount and distribution of Au, and determined  
111 the local environment of Au using XAS. An *in situ* heating experiment was performed to  
112 estimate the effect of metamorphism on chemically bound Au in pyrite. The experimental data  
113 were combined with first-principles quantum chemical calculations and Bader charge analysis in  
114 order to reveal the local atomic environment and oxidation state of Au in pyrite, arsenopyrite,  
115 and löllingite.

116  
117

## Methods

118 **Mineral synthesis and analytical methods**

119           Synthesis experiments were performed using hydrothermal (450 °C, 1 kbar) and salt flux  
120 (520 – 650 °C) methods. Saturation with respect to Au<sub>(cr)</sub> was achieved in all experiments by  
121 placing a piece of Au foil or wire in the autoclave or silica glass ampoule together with initial  
122 reagents. The hydrothermal method was used for pyrite synthesis only; the salt flux method was  
123 employed to obtain crystals of Au-bearing pyrite, arsenopyrite, and löllingite. The chemical  
124 composition of the synthesized phases was determined by electron microprobe analysis (EPMA)  
125 and laser ablation inductively coupled plasma mass spectrometry (LA-ICP-MS). The chemical  
126 composition of hydrothermal pyrite was determined by wet chemistry. Details of the synthesis  
127 procedures and analytical methods are given in Supplementary Methods.

128

129 **X-ray absorption spectroscopy (XAS)**

130           XAS spectra of Au-bearing pyrite, arsenopyrite, löllingite, and other substances (Au foil  
131 and synthetic Au<sub>2</sub>S, AuSb<sub>2</sub> and Au<sub>2</sub>Bi) were collected at high-brilliance X-ray absorption and X-  
132 ray emission spectroscopy undulator beamline ID26 (Gauthier et al., 1999) of the European  
133 Synchrotron Radiation Facility (ESRF) at Grenoble. The incident energy was selected using the  
134 <111> reflection from a double Si crystal monochromator. The rejection of higher harmonics  
135 was achieved by three Cr/Pd mirrors positioned at an angle of 2.5 mrad relative to the incident  
136 beam. The flux of the incident X-ray beam was approximately  $2 \cdot 10^{13}$  photon s<sup>-1</sup> on the sample  
137 position. XANES spectra were simultaneously measured in the total fluorescence yield (TFY)  
138 mode using a photodiode and in the high energy resolution fluorescence detection (HERFD)  
139 mode using an X-ray emission spectrometer (Glatzel and Bergmann, 2005; Kvashnina and  
140 Scheinost, 2016). The sample, analyzer crystal, and photon detector (silicon drift diode) were  
141 arranged in a vertical Rowland geometry. The Au XANES/EXAFS HERFD spectra at the L<sub>3</sub>  
142 edge were obtained by recording the intensity of the Au L $\alpha_1$  emission line (9713 eV) as a

143 function of the incident energy. The emission energy was selected using the  $\langle 660 \rangle$  reflection of  
144 four spherically bent Ge crystal analyzers (1 m curvature radius) aligned at  $80^\circ$  Bragg angle. A  
145 combined (incident convoluted with emitted) energy resolution of 1.2 eV was determined by  
146 measuring the elastic peak. The intensity was normalized to the incident flux.

147 For the heating experiment, a powder of hydrothermal pyrite was loaded into a silica  
148 glass capillary (Polymicro Technologies<sup>TM</sup>, 350  $\mu\text{m}$  OD, 200  $\mu\text{m}$  ID, 20 mm length) together  
149 with a small amount of sulfur, which prevented sample oxidation and fixed sulfur fugacity  $f(\text{S}_2)$   
150 during the experiment. The capillary was evacuated and hermetically sealed. This simple  
151 experimental technique was developed by Chou et al. (2008, 2012) and Ding (2010) for the  
152 Raman spectroscopy of solids and liquids, and we adopted it for the synchrotron experiment. For  
153 *in situ* XAS measurements, the capillaries were placed into a microtomography furnace (Bellet et  
154 al., 2003). Temperature was measured by a K-type thermocouple in contact with the capillary at  
155 an accuracy of  $\pm 5^\circ\text{C}$ .

156

### 157 **Density Functional Theory (DFT) calculations**

158 The QUANTUM ESPRESSO software package (Giannozzi et al., 2009) was used for  
159 quantum chemical DFT calculations. We employed a projector-augmented wave (PAW) all-  
160 electron description of electron-ion-core interactions (Blöchl, 1994; Kresse, 1999) and the  
161 Perdew-Burke-Ernzerhof (PBE) exchange-correlation functional. For the electronic structure  
162 calculations, the self-consistent field (SCF) method was applied with a 100 Ry kinetic energy  
163 cutoff for the plane waves, a 1500 Ry charge density cutoff, and an SCF tolerance better than  $10^{-9}$ .  
164 The relaxation of atomic positions and cell parameters was performed in a supercell containing  
165  $2 \times 2 \times 2$  unit cells for the pyrite and arsenopyrite, and  $2 \times 2 \times 3$  unit cells for the löllingite. The  
166 crystal structure and supercell parameters were optimized using the BFGS algorithm for atomic  
167 coordinates with a convergence threshold of  $10^{-3}$  Ry/au for forces and  $10^{-4}$  Ry for energy.

168 Topological atomic charges were determined from the quantum theory of atoms in molecules  
169 (QTAIM). The local atomic charges were calculated by integrating the charge density within  
170 Bader volumes around the atoms (Otero-de-la-Roza et al., 2009, 2014).

171

## 172 **EXAFS spectra analysis**

173 The analysis of EXAFS spectra provided insight into the Au local atomic environment.  
174 The EXAFS data ( $\chi_{exp}(k)$ ) were analyzed using the IFEFFIT software package (Ravel and  
175 Newville, 2005). After the standard procedures of pre-edge subtraction and spline background  
176 removal, interatomic distances ( $R_i$ ), coordination numbers ( $N_i$ ), and Debye–Waller factors ( $\sigma^2$ )  
177 were determined by the non-linear fitting of experimental data with the theoretical spectrum  
178 described by the equation

$$179 \quad \chi(k) = S_0^2 \sum_{i=1}^n \frac{N_i F_i(k)}{R_i^2 k} e^{\frac{-2R_i}{\lambda(k)}} e^{-2\sigma_i^2 k^2} \sin(2kR_i + \phi_i(k)) \quad . \quad (1)$$

180 The parameters necessary for the simulation of the theoretical spectra (photoelectron mean free  
181 path  $\lambda(k)$ , amplitude  $F_i(k)$ , phase shift  $\phi_i(k)$ ) were calculated *ab initio* using the FEFF6 program  
182 (Zabinsky et al., 1995). The statistical uncertainty of the calculation method is 0.01–0.02 Å for  
183 refined  $R_i$  in the first coordination shell.

184

## 185 **XANES spectra simulation**

186 Theoretical calculations of Au L<sub>3</sub> edge XANES spectra were performed using two  
187 approaches: finite difference method (FDM) and full multiple scattering (FMS). The FDM is  
188 implemented in the FDMNES code (Joly, 2001; Guda et al., 2015). Relativistic self-consistent  
189 field FDMNES calculations were carried out with the exchange-correlation part of the potential  
190 in a local density approximation (Hedin and Lundqvist, 1971). The final electronic states were  
191 calculated in a full core hole screening. Atomic clusters inside the spheres with radii of 8 Å and 7



192 Å were chosen for self-consistent calculations and FDM XANES calculations, respectively. To  
193 account for many body effects and core hole lifetime broadening, the arctangent convolution was  
194 applied (Bunău and Joly, 2009). Although the FDMNES procedure is computationally  
195 expensive, it is best for systems with non-spherical charge distribution.

196 The FMS spectra modeling was performed using the FEFF9.6 revision 4 code (Rehr et  
197 al., 2010), which is based on the self-consistent muffin-tin potentials. The Dirac-Hara exchange-  
198 correlation potentials were used. The parameter for the imaginary potential was set to -2 to  
199 account for the reduced broadening of HERFD-XANES spectra. Self-consistent calculations  
200 were refined with a radius of 6 Å around the central Au atom, whereas a radius of 7 Å was  
201 chosen for FMS calculations. The RPA core hole approximation was applied to simulate the  
202 central excited atom.

203  
204

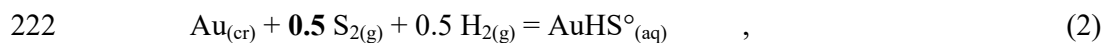
## Results

### 205 Au content and distribution in synthesized minerals

206 **Pyrite FeS<sub>2</sub>.** The contents of Au in the hydrothermal pyrites and coexisting aqueous fluid  
207 (450 °C, 1 kbar) are presented in Supplementary Table S1. The hydrothermal pyrite is a fine-  
208 grained aggregate of particles <10 µm in size (Fig. 1a). The powder is free of metallic Au and,  
209 therefore, the total Au content determined by the dissolution of the pyrite samples corresponds to  
210 “invisible” Au. We note here that the synthesis of pyrite free of metallic Au inclusions was  
211 possible only in acidic solutions with a low concentration of dissolved Au. Our attempts to  
212 increase the content of “invisible” Au in pyrite using weakly alkaline solutions with high  
213 aqueous Au concentrations (up to 0.1 mol·kg H<sub>2</sub>O<sup>-1</sup>, or 2·10<sup>5</sup> ppm) yielded a mixture of pyrite  
214 and Au metal (Fig. S1). The content of Au in pure FeS<sub>2</sub> grains obtained in these experiments was  
215 close to the EPMA detection limit of 100 ppm.

216 Sulfur fugacity was buffered in the hydrothermal experiments owing to elemental sulfur  
217 dissolution and hydrolysis reactions (see Supplementary Methods). The concentration of Au in

218 aqueous fluid increases with increasing  $f(S_2)$  (Fig. 1b). The slope of the linear fit of the  
219 experimental Au solubility vs.  $f(S_{2(g)})$  is  $S = 0.67$  in the logarithmic scale. This means that  
220  $AuHS^{\circ}_{(aq)}$  dominates aqueous Au speciation. For this complex  $S = 0.5$ , which is consistent with  
221 the reaction



223 because  $f(H_{2(g)})$  is the same for all experimental points (except for the  $S + H_2SO_4$  experiment).  
224 The observed increase of the slope could be caused by the presence of  $Au(HS)_2^-$  and/or  
225 uncertainty of the calculated  $f(S_{2(g)})$  values.

226 The effect of  $f(S_{2(g)})$  on the content (solubility) of Au in solid sulfide determines the  
227 stoichiometry of the solubility reaction (number of  $S_2$  molecules interacting with Au to form Au-  
228 bearing sulfide)



230 and, therefore, the Au/S ratio and the formal oxidation state of Au in the sulfide. In contrast to  
231 the Au solubility in aqueous fluid, the content of Au in hydrothermal pyrite is weakly sensitive to  
232  $f(S_2)$  and oxidation potential and always falls within the 40 – 90 ppm range (Table S1). We  
233 consider a value of ~100 ppm as an upper Au concentration limit for the  $T/P$  conditions of the  
234 synthesis experiments. Formally, the slope  $S \sim 0$  may indicate that Au does not interact with  
235 dissolved sulfur and, therefore, the Au oxidation state in the sulfide remains unchanged.  
236 However, the real structural position and valence state of Au distributed in the sulfide mineral  
237 matrix could be determined only by spectroscopic experiments described in the following  
238 section.

239 Grains of high-temperature pyrite synthesized at 620 °C using the salt flux method show  
240 zonal Au distribution with  $C(Au)$  ranging from the LA-ICP-MS detection limit to several  
241 hundred ppm (Table S2). The smooth character of the Au time-resolved LA-ICP-MS spectra  
242 (Fig. S2) suggests that microscopic and submicroscopic inclusions of Au are absent. It is

243 interesting that, in addition to Au, this pyrite sample contains several ppm Pt, which was  
244 accidentally introduced into the charge.

245 **Arsenopyrite FeAsS and löllingite FeAs<sub>2</sub>.** Examples of arsenopyrite and löllingite  
246 crystals are shown in Supplementary Figs. S3 and S4, respectively. Two types of LA-ICP-MS  
247 spectra were obtained for the arsenopyrite. The first type shows Au-rich (hundreds of ppm) and  
248 Au-poor (up to 30 ppm) zones (top of Fig. S5), and the second type corresponds to  
249 homogeneously distributed Au at  $C(\text{Au}) \sim 10 \div 30$  ppm (Fig. S5, bottom). In the löllingite Au is  
250 distributed homogeneously at  $C(\text{Au}) = 800 \pm 300$  ppm (Fig. S6).

251

## 252 XANES spectroscopy

253 **Ambient temperature experiment.** The HERFD-XANES spectroscopic technique could  
254 be used to acquire Au L<sub>3</sub> edge spectra not only for pyrite but also for arsenopyrite and löllingite,  
255 in which the signal from the trace amount of “invisible” Au is masked by the As K edge in the  
256 TFY mode (Fig. 2). Another advantage of this technique is that the weak features of Au(I)  
257 spectra are considerably enhanced compared with TFY spectra, which facilitates interpretation  
258 and modeling. Figure 3a shows Au L<sub>3</sub> edge HERFD-XANES spectra of Au-bearing pyrite  
259 (hydrothermal), arsenopyrite, and löllingite together with spectra of model substances. All these  
260 minerals contain Au in the chemically bound state that is different from both Au<sub>(cr)</sub> and Au<sub>2</sub>S.  
261 The positions of the edge jump (e.j.) and the first intense feature (white line, WL) are given in  
262 Table 1. We observed a significant positive energy shift of the e.j. position increasing in the  
263 order pyrite < arsenopyrite < löllingite. A positive e.j. shift usually indicates an increase in the  
264 positive charge of the excited atom. However, we will show below that this is not the case for the  
265 Fe-As-S system.

266 The Au L<sub>3</sub> edge absorption is related to  $2p\text{-}5d$  dipole-allowed transitions:  $2p_{3/2} \rightarrow$   
267  $5d_{5/2}/5d_{3/2}$ . Therefore, the WL intensity reflects the number of empty states in the  $5d_{5/2}$  and  $5d_{3/2}$

268 orbitals above the Fermi level. The WL intensity for arsenopyrite and löllingite is much greater  
269 than that for pyrite (Fig. 3a), indicating a higher number of holes in the  $5d$  electronic shell of As-  
270 bearing minerals. Another important characteristic of the Au  $L_3$  edge HERFD-XANES spectra of  
271 these minerals is the negative correlation between the intensity of the second feature at  $\sim 11929$   
272 eV and As content. This can be clearly seen in the spectra of Au-bearing pyrite, the arsenopyrite  
273 spectra contain only traces of the feature, and it is absent in the löllingite spectra.

274 A comparison of the spectra of arsenopyrite and löllingite with those of synthetic  $\text{AuSb}_2$   
275 and  $\text{Au}_2\text{Bi}$  revealed a significant positive shift of the e.j. position increasing in the order  $\text{Au}_2\text{Bi} <$   
276  $\text{AuSb}_2 < \text{Au}$  in arsenopyrite  $< \text{Au}$  in löllingite (Fig. 3b, Table 1). This order corresponds to a  
277 decrease in the number of the chemical element in the 15<sup>th</sup> group of the periodic system and  
278 implies that Au is chemically bound to As in the arsenopyrite and löllingite matrices.

279 **Pyrite heating experiment.** This experiment (Fig. 4) was aimed at modeling the  
280 behavior of chemically bound “invisible” Au during hydrothermal ore metamorphism. The  
281 spectra collected at ambient temperature indicate different chemical states of Au in hydrothermal  
282 and salt flux pyrites. Chemically bound “invisible” Au exists only in the hydrothermal pyrite.  
283 Well-crystallized large pyrite grains formed in the eutectic anhydrous chloride mixture contain  
284 mostly metallic  $\text{Au}^0$ . Heating of the hydrothermal pyrite to  $460\text{ }^\circ\text{C}$  results in the decomposition  
285 of the Au-bearing phase and precipitation of  $\text{Au}^0$ . Note that this process takes place even in the  
286 presence of  $\text{S}_{(\text{liq})}$ , which should promote the formation of an Au-bearing solid solution (Eq. 3).  
287 Further heating to  $630\text{ }^\circ\text{C}$  results in a dramatic drop of the XAFS signal; the spectrum collected  
288 at this temperature indicates traces of chemically bound Au. This can be explained by the  
289 coalescence of Au nanoparticles. These data are consistent with the analyses of natural Au-  
290 bearing arsenopyrite reported by Wagner et al. (2007), which showed that metamorphism caused  
291 Au depletion in arsenopyrite. The irreversible coarsening of Au nanoparticle during arsenian  
292 pyrite heating was observed by means of in situ transmission electron microscopy (Reich et al.,

293 2006). Our results demonstrate that the heating (metamorphism) of Au-bearing pyrite results in  
294 the decomposition of chemically bound “invisible” Au incorporated into the hydrothermal pyrite  
295 matrix during ore formation.

296

### 297 **EXAFS analysis**

298 The EXAFS spectra of pyrite and löllingite are shown in Fig. 5. Contamination with  
299 metallic Au<sup>0</sup> hampered the collection of good quality EXAFS spectra for arsenopyrite; therefore,  
300 only the XANES region was used to characterize the chemical state of Au in this mineral. The  
301 EXAFS spectra of pyrite and löllingite (Fig. 5, top) are different: the maxima of the EXAFS  
302 function of the latter are clearly shifted to higher  $k$  values. The main peak in the Fourier  
303 transforms (FTs) of the löllingite EXAFS function (Fig. 5, bottom) lies at higher  $R$  values,  
304 reflecting a larger Au-L distance in the first coordination shell. The results of the least-squares fit  
305 of the FTs are shown by thick red lines in Fig. 5, and the calculated model parameters are given  
306 in Table 2. For both minerals, the best fit of the experimental spectra is achieved for Au  
307 occupying the position of Fe in the mineral structure. In these minerals (see Supplementary  
308 Structures), the metal atom is octahedrally coordinated. In the structure of pyrite, the first  
309 neighbors of Au are 6 S atoms at 2.40 Å distance; in the structure of löllingite, 6 As atoms at  
310 2.52 Å. Due to the large Au ionic radius, the Au-L distances increase by 0.14 Å and 0.16 Å  
311 relative to the crystal structures of pure pyrite and löllingite. Fitting of the first coordination shell  
312 of Au yielded  $N = 5.9 \pm 1.5$  and  $5.3 \pm 0.8$  for pyrite and löllingite, respectively, confirming the  
313 octahedral coordination of Au in these minerals. The distortion of the local environment around  
314 Au in pyrite decreases to 0.06 – 0.08 Å for S atoms in the second coordination shell, and the Au-  
315 Fe distance for the nearest Fe atoms at  $\sim 3.8$  Å remains almost unchanged (within 0.04 Å).  
316 Similar relations are observed for löllingite: the distortion of the crystalline structure decreases  
317 for distant coordination shells and disappears at  $R > 4.2$  Å.

318

### 319 **DFT calculations**

320 Interatomic distances optimized by the DFT method for pyrite and löllingite are given in  
321 Table 2. In the case of löllingite, good agreement is observed between the simulated structure  
322 and the results of the EXAFS spectra fitting for the first and second neighbors ( $\pm 0.02$  Å for the  
323 first coordination shell at 2.5 Å and  $\pm 0.03$  Å for the second shell at 3 Å). Similar results were  
324 obtained in our recent study of Au-bearing covellite CuS, the EXAFS model of which was  
325 adequately reproduced by DFT simulation at distances up to 4 Å (agreement between DFT  
326 calculations and EXAFS fitting was within 0.01 – 0.04 Å depending on the distance) (Tagirov et  
327 al., 2016). Based on these results, we can suggest that our method of DFT calculation reproduces  
328 the atomic coordinates of Au-bearing chalcogenides within  $\pm 0.02$  and 0.04 Å, at least for the first  
329 two coordination shells located at distances up to 3 Å.

330 In the case of pyrite, the agreement between the DFT simulation and EXAFS fit is poor:  
331 the difference is 0.055 Å for the first neighbors around Au atom. This fact can be explained by  
332 the thermodynamic instability of Au-bearing pyrite, the structure of which cannot be accurately  
333 reproduced by equilibrium structure relaxation methods. This inference is consistent with the  
334 results of the pyrite heating experiment, in which chemically bound Au was decomposed at high  
335 temperature and escaped from the FeS<sub>2</sub> matrix. This is opposite to the general rule that an  
336 increase in temperature tends to stabilize solid solutions.

337 Table 3 reports the results of the DFT simulation of the local atomic environment of Au-  
338 bearing arsenopyrite. The distances Au-S and Au-As in the first coordination shell increase by  
339 0.13 Å and 0.23 Å, respectively. The Au-Fe distance for the nearest two Fe atoms increases by  
340 0.25 Å relative to pure arsenopyrite. This model was checked by the results of Au L<sub>3</sub> edge  
341 HERFD-XANES spectra simulation, which is described below.

342

### 343 **XANES spectra simulation**

344           The results of Au L<sub>3</sub> edge HERFD-XANES spectra modeling are shown in Fig. 6a-c. The  
345 FDMNES simulation of Au in pyrite spectrum (Fig. 6a) overestimates the WL intensity and  
346 shifts the second feature by ~2 eV relative to the experimental spectrum. This disagreement  
347 probably stems from the metastable nature of “invisible” Au in pyrite, which leads to  
348 discrepancies in FDM SCF-based spectra modeling. The spectrum calculated using the FEFF9  
349 computer code is given for comparison. The agreement between the experimental and simulated  
350 spectra is good, with the exception of the third diffuse feature with a centroid at ~11945 eV,  
351 which is absent in the calculated spectrum.

352           The simulated spectrum of löllingite is in good agreement with the experimental one (Fig.  
353 6b). The only difference is the overestimated width of WL. The intensity and positions of the  
354 spectral features for Au-bearing arsenopyrite are correctly reproduced by the FDMNES  
355 calculation (Fig. 6c), which supports our results of DFT calculation for this mineral.

356           Theoretical FDMNES calculations showed that the second feature in the spectra of Au  
357 bearing pyrite and arsenopyrite (at ~11929 eV) originates mostly from the mixing of hybridized  
358 Au *p,d* and S *p* orbitals. At this energy, the contribution of As *p* empty valence states to chemical  
359 bond formation is weak for arsenopyrite and negligible for löllingite. This is why the second  
360 feature is intense in the spectra of Au-bearing pyrite and absent in the löllingite spectra.

361           Despite the fact that both the FDMNES and FEFF programs calculate charge states using  
362 the muffin-tin approximation, the FEFF code is known to be more efficient for systems with  
363 isotropic potential compared with systems with anisotropic potential, whereas the FDMNES  
364 program successfully reproduces charge states and spectral features in systems of both types.  
365 The fact that the theoretical spectra of Au-bearing pyrite obtained by the FEFF code are in close  
366 agreement with the experimental Au L<sub>3</sub> edge XANES is indicative of a highly symmetric  
367 environment (octahedral) of Au in pyrite, rather than a linear coordination like that in Au<sub>2</sub>S.

368

### 369 **The valence state of “invisible” Au**

370 The results of the Bader analysis of electron density performed using QTAIM for the  
371 pure and Au-bearing minerals are summarized in Table 4. The partial atomic charge of S in  
372 pyrite is more negative than that of As in löllingite (-0.7 e for disulfide group in pyrite vs. -0.08 e  
373 for As in löllingite). The topological charge of As in arsenopyrite is +0.18 e, whereas S is  
374 negatively charged (-0.6 e). These atomic partial charges reflect the distribution of delocalized  
375 electrons and are in line with Pauling electronegativity:  $\chi(\text{S}) = 2.58 \gg \chi(\text{As}) = 2.18$  (Huheey et  
376 al., 2000). In the Au-bearing minerals discussed here, the atomic charge of Au increases in the  
377 order löllingite < arsenopyrite < pyrite. Au is positively charged in the pyrite, nearly neutral in  
378 the arsenopyrite, and negatively charged in the löllingite. Note that the charge of Au in the  
379 löllingite is much more negative than that of As. This is explained by the fact that Au is the most  
380 electronegative metal ( $\chi(\text{Au}) = 2.54$ ) whose electron affinity is higher than that of semi-metals.

381

### 382 **Discussion and implications**

383 The results of our study demonstrate that Au substitutes for Fe in the crystal structures of  
384 pyrite, arsenopyrite, and löllingite. However, the chemical nature of “invisible” Au in these  
385 minerals is different. In pyrite, chemically bound Au is formed only in the presence of  
386 hydrothermal solution. This is consistent with the results of Widler and Seward (2002) on Au  
387 adsorption by pyrite. They found that Au can be efficiently scavenged by natural and synthetic  
388 pyrites from acidic aqueous solutions in which  $\text{AuHS}^{\circ}_{(\text{aq})}$  is the dominant Au complex. Similar  
389 Au adsorption isotherms were observed for  $\text{As}_2\text{S}_3$  and  $\text{Sb}_2\text{S}_3$  by Renders and Seward (1989). In  
390 view of these results, our observation of independence of Au concentration in pyrite on  $f(\text{S}_2)$   
391 (and, consequently, on  $\text{AuHS}^{\circ}_{(\text{aq})}$  concentration) can be attributed to the attainment of the  
392 maximum pyrite sorption capacity with respect to Au. In contrast, pyrite grains synthesized in a

16



393 dry salt melt contain only Au<sup>0</sup>. Furthermore, heating of hydrothermal pyrite in a dry system  
394 results in the decomposition of chemically bound Au.

395 The XPS measurements by Widler and Seward (2002) on Au-bearing pyrites showed that  
396 the chemical state of Au in pyrite is different from Au<sup>0</sup>. The Au 4f<sub>7/2</sub> electron binding energy  
397 (BE) is 84.8 eV for Au in pyrite, whereas BE = 84.0 eV for metallic Au. A similar value of BE =  
398 85.1 eV was obtained for Au-bearing pyrite synthesized at 200 °C (Laptev and Rozov, 2006).  
399 This value is higher than Au 4f<sub>7/2</sub> BE in Au<sub>2</sub>S, where Au is linearly coordinated with two S atoms  
400 (BE<sub>Au/Au<sub>2</sub>S</sub> ~84 eV, Tagirov et al., 2014) implying different local environments of Au in pyrite  
401 and Au<sub>2</sub>S. However, the core level XPS technique is less sensitive to local atomic environment  
402 geometry and chemical bonding compared to XAFS spectroscopy, which is appropriate for  
403 reliable determination of the chemical state of Au.

404 The present study and experimental investigations of Au-bearing As-free pyrites (Fadeev  
405 and Kozerenko, 1999; Kozerenko et al., 2001; Widler and Seward, 2002; Laptev and Rozov,  
406 2006) combined with data on Au contents in sulfide ores from different geologic environments,  
407 suggest that pyrite can efficiently uptake Au even in As-poor systems, if large amounts of  
408 hydrothermal ore are rapidly formed. Such a process may occur, for example, in hydrothermal  
409 black smoker systems where fine-grained sulfides are formed owing to the mixing of  
410 hydrothermal solutions with cold oxidized seawater (Bortnikov et al., 2003; Grichuk, 2012). The  
411 content of chemically bound “invisible” Au in As-free pyrite determined in the present study for  
412 450 ° (tens of ppm) is somewhat lower than the maximum values of ~100 ppm measured in  
413 pyrite synthesized at 200 °C (Laptev and Rozov, 2006) and ~100 - 300 ppm in the ambient-  
414 temperature sorption experiments of Widler and Seward (2002). Neglecting differences in  
415 surface area or grain size, which is usually within 1-10 μm for fine-grained pyrite, the  
416 maximum content of chemically bound Au in As-free hydrothermal pyrite formed at 25-450 °C  
417 can be estimated as 30 ppm < C(Au) < 300 ppm. A temperature increase tends to reduce the Au

418 content, which is partly compensated by the stabilization and enrichment of  $\text{AuHS}^{\circ}_{(\text{aq})}$  in high-  
419 temperature solution/fluid (Stefánsson and Seward, 2004). The maximum content of chemically  
420 bound “invisible” Au in hydrothermal pyrite can be roughly estimated as 100-300 ppm at 25 °C,  
421 ~150 ppm at 100 °C, ~100 ppm at 200 °C, and 100-50 ppm at 300-500 °C; a retrograde behavior  
422 is thus evident. One should expect that excess Au will be present in the metallic state. This  
423 behavior of “invisible” Au in synthetic pyrite is consistent with published data on natural  
424 minerals (e.g. Fig 9a in Deditius et al., 2014).

425 In contrast to pyrite, Au can form an isomorphous solid solution in arsenopyrite and  
426 löllingite even at high temperatures (> 500°C) in the absence of aqueous fluid. This suggests a  
427 thermodynamic stability of this form of chemically bound Au in these minerals. The maximum  
428 content of chemically bound “invisible” Au is tens ppm for arsenopyrite and hundreds ppm for  
429 löllingite. Our data are consistent with natural observations, which show that As stabilizes Au-  
430 bearing sulfides and leads to an increase in Au content (c.f., Reich et al., 2005; Deditius et al.,  
431 2014). Further insight into the speciation of chemically bound Au can be drawn from the fact  
432 that As substitutes for S in pyrite with formation of an isomorphous solid solution showing  
433 significant clustering of As atoms (Zotov et al., 1972, Savage et al., 2000; Reich and Becker,  
434 2006). However, more spectroscopic data are necessary to determine unambiguously the  
435 chemical state of As and Au in arsenian pyrite.

436 A comparison of the Au  $L_3$  edge HERFD-XANES spectra shows that edge energy (e.j.)  
437 increases when As replaces S in the order pyrite < arsenopyrite < löllingite (Table 1, Fig. 3a).  
438 Usually, the atomic charge increases in the same order, becoming more positive at higher e.j.  
439 (higher energy is necessary to excite the core level electron). However, the data in Table 4 show  
440 that the opposite is true: the Au charge is positive in pyrite and negative in löllingite. Such an e.j.  
441 behavior cannot be explained by the effect of the atomic charge alone and needs further  
442 examination.

443           The WL position and intensity indicate that the number of Au *5d* unoccupied electronic  
444 states increases in As-bearing phases relative to pyrite, despite the fact that Au is more  
445 electronegative than As. This peculiarity can be explained by the charge compensation model  
446 describing the charge flow in Au alloys (Watson et al., 1971). In this model, the Au *d*-charge loss  
447 upon alloying is overcompensated by conduction (mainly *s-p*) charge gain from the second alloy  
448 component. As a result, Au gains an overall negative charge (see Kuhn and Sham, 1994;  
449 Bzowski et al., 1995, and reference therein).

450           The fact that the valence state of Au can vary depending on the host mineral composition  
451 (Table 4) demonstrates that coupled charge-compensation substitution is not necessary for the  
452 formation of isomorphous solid solutions in crystals with highly covalent chemical bonds.

453           Along with Au, other noble metals (platinum group elements, Ag) often occur as an  
454 “invisible” admixture in sulfide ore (c.f., Filimonova et al., 2015, and reference therein).  
455 Considering their chemical state in sulfide minerals from the point of view of our study, we  
456 suggest that these metals can also form a chemically bound refractory admixture. The chemical  
457 state and the concentration of this form of noble metals can vary with the local atomic  
458 environment/structural position and valence state depending on the composition of host sulfide  
459 and ore origin (e.g., hydrothermal, magmatic, or metamorphic). Further spectroscopic studies,  
460 including in situ X-ray absorption/emission spectroscopy at high *T/P* parameters, will help to  
461 determine the chemical state of noble metals and mechanisms of ore-forming processes.

462

463 **Acknowledgments:** The authors acknowledge ESRF for allocating beamtime under proposals  
464 ES-184 and ES-360. The help and support of Sara Lafuerza and Pieter Glatzel during the  
465 beamtime is greatly appreciated. B.R.T. and K.O.K. thank Hugo Vitoux for outstanding technical  
466 support during the in-situ experiment with micro-furnace at the ID26 beamline. We are grateful  
467 to Sara-J. Barnes for organizing the LA-ICP-MS measurements at the University of Chicoutimi,

468 V. Abramova and E. Minervina for the LA-ICP-MS analysis of synthesized minerals. We are  
469 grateful to Andrey Giris and Anastasia Plyasunova for correction of English grammar. We  
470 thank Barbara Etschmann, Martin Reich, and an anonymous reviewer for helpful comments and  
471 suggestions. The results of this work were obtained using the computational resources of MCC  
472 NRC “Kurchatov Institute” (<http://computing.kiae.ru/>). This study was supported by the Russian  
473 Scientific Foundation, grant No. 14-17-00693. D.Ch was involved in Act 211 Government of the  
474 Russian Federation, agreement № 02.A03.21.0006 (synthesis of sulfides via salt flux technique).  
475

476

### References cited

- 477 Bayliss, P. (1977) Crystal structure refinement of weakly anisotropic pyrite cubic model.  
478 American Mineralogist, 62, 1168-1172.
- 479 Bellet, D., Gorges, B., Dallery, A., Bernard, P., Pereiro, E., and Baruchel, J. (2003) A  
480 1300 K furnace for in situ X-ray microtomography. Journal of Applied Crystallography, 36, 366-  
481 367.
- 482 Bindi, L., Moelo, Y., Leone, P., and Suchaud, M. (2012) Stoichiometric arsenopyrite,  
483 FeAsS, from La Roche-Balue Quarry, Loire-Atlantique, France: Crystal structure and Mossbauer  
484 study. The Canadian Mineralogist, 50, 471-479.
- 485 Blöchl, P.E. (1992) Projector augmented-wave method. Physical Review B, 50, 17953-  
486 17979.
- 487 Bortnikov, N.S., Cabri, L.J., Vikentiev, I.V., Tagirov, B.R., Mc Mahon, G., Bogdanov,  
488 Yu.A., and Stavrova, O.O. (2003) Invisible gold in sulfides from seafloor massive sulfide  
489 edifices. Geology of Ore Deposits, 45, No. 3, 201-212.
- 490 Bunău O., and Joly Y. (2009) Self-consistent aspects of x-ray absorption calculations.  
491 Journal of Physics: Condensed Matter, 21, 345501.
- 492 Bzowski, A., Yiu, Y.M., and Sham, T.K. (1995) Charge redistribution in Au-metalloid  
493 intermetallics: A Au  $L_{2,3}$ -edge X-ray absorption study. Physical Review B, 51, 9515-9520.
- 494 Cabri, L.J., Newville, M., Gordon, R.A., Daryl Crozier, E., Sutton, S.R., McMahon, G.,  
495 and Jiang, D.T. (2000) Chemical speciation of gold in arsenopyrite. The Canadian Mineralogist,  
496 38, 1265-1281.
- 497 Cardile, C.M., Cashion, J.D., McGrath, A.C., Renders, P., and Seward, T.M. (1993)  $^{197}\text{Au}$   
498 Mössbauer study of  $\text{Au}_2\text{S}$  and gold adsorbed onto  $\text{As}_2\text{S}_3$  and  $\text{Sb}_2\text{S}_3$  substrates. Geochimica et  
499 Cosmochimica Acta, 57, 2481-2486.

- 500 Chou, I-M. (2012) Optical cells with fused silica windows for the study of geological  
501 fluids. In J. Dubessy, M.-C. Gaumont and F. Rull Eds., Applications of Raman Spectroscopy to  
502 Earth Sciences and Cultural Heritage, 12, p. 227-248. EMU Notes in Mineralogy, London.
- 503 Chou, I-M., Song, Y., and Burruss, R. C. (2008) A new method for synthesizing fluid  
504 inclusions in fused silica capillaries containing organic and inorganic material. *Geochimica et*  
505 *Cosmochimica Acta*, 72, 5217-5231.
- 506 Cook, N.J., Ciobanu, C.L., and Mao, J. (2009) Textural control on gold distribution in As-  
507 free pyrite from the Dongping, Huangtuliang and Hougou gold deposits, North China Craton  
508 (Hebei Province, China). *Chemical Geology*, 264, 101-121.
- 509 Deditius, A.P., Reich, M., Kesler, S.E., Utsunomiya, S., Chryssoulis, C.L., Walshe, J., and  
510 Ewing, R.C. (2014) The coupled geochemistry of Au and As in pyrite from hydrothermal ore  
511 deposits. *Geochimica et Cosmochimica Acta*, 140, 644-670.
- 512 Ding, J. (2010) The pH determination of palaeofluids: experimental and thermodynamic  
513 approach, 173 p. PhD thesis, Université Henri Poincaré, Nancy.
- 514 Fadeev, V.V., and Kozerenko, S.V. (1999) Gold in processes of pyrite formation. Part 1.  
515 Gold accumulation during pyrite formation. *Geochemistry International*, No. 12, 1182-1190.
- 516 Filimonova, O.N., Minervina, E.A., Kovalchuk, E.A., Abramova, V.D., Vikent'iev, I.V.,  
517 Tagirov, B.R., Chareev, D.A., and Chvosticov, V.A. (2015) An experimental study of noble and  
518 base metals (Au, Ag, Pt, Pd, Zn) distribution in pyrite and pyrrhotite. In A.-S. André-Meyer et  
519 al., Eds., Proceedings of the 13<sup>th</sup> Biennial SGA Meeting, Mineral Resources in a Sustainable  
520 World, p. 925-927. Nancy, France.
- 521 Franchini, M., McFarlane, C., Maydagán, L., Reich, M., Lentz, D.R., Meinert, L., Bouhier,  
522 V. (2015) Trace metals in pyrite and marcasite from the Agua Rica porphyry-high sulfidation  
523 epithermal deposit, Catamarca, Argentina: Textural features and metal zoning at the porphyry to  
524 epithermal transition. *Ore Geology Reviews*, 66, 366–387.

- 525 Gauthier, C., Sole, V.A., Signorato, R., Goulon, J., and Moguiline, E. (1999) The ESRF  
526 beamline ID26: X-ray absorption on ultra dilute sample. *Journal of Synchrotron Radiation*, 6,  
527 164-166.
- 528 Genkin, A.D., Bortnikov, N.S., Cabri, L.J., Wagner, F.E., Stanley, C.J., Safonov, O.G.,  
529 McMahon, G., Friedl, J., Kerzin, A.L., and Gamyranin, G.N. (1998) A multidisciplinary study of  
530 invisible gold in arsenopyrite from four mesothermal gold deposits in Siberia, Russian  
531 federation. *Economic Geology*, 93, 463-487.
- 532 Giannozzi, P., Baroni, S., Bonini, N., Calandra, M., Car, R., Cavazzoni, C., Ceresoli, D.,  
533 Chiarotti, G.L., Cococcioni, M., Dabo, I. and others (2009) QUANTUM ESPRESSO: a modular  
534 and open-source software project for quantum simulations of materials. *Journal of Physics:*  
535 *Condensed Matter*, 21, 395502.
- 536 Glatzel, P., and Bergman, U. (2005) High resolution 1s core hole X-ray spectroscopy in 3d  
537 transition metal complexes - electronic and structural information. *Coordination Chemistry*  
538 *Reviews*, 249, 65-95.
- 539 Goldfarb, R.J., Baker, T., Dube, B., Groves, D.I., Hart, C.J., and Gosselin, P. (2005)  
540 Distribution, character, and genesis of gold deposits in metamorphic terranes. *Economic*  
541 *Geology 100th Anniversary Volume*, 407-450.
- 542 Guda, S.A., Guda, A.A., Soldatov, M.A., Lomachenko, K. A., Bugaev, A. L., Lamberti, C.,  
543 Gawelda, W., Bressler, C., Smolentsev, G., Soldatov, A.V., and Joly, Y. (2015) Optimized finite  
544 difference method for the full-potential XANES simulations: application to molecular adsorption  
545 geometries in MOFs and metal-ligand intersystem crossing transients. *Journal of Chemical*  
546 *Theory and Computation*, 11, 4512-4521.

- 547 Grichuk, D.V. (2012) Thermodynamic model of ore-forming processes in a submarine  
548 island-arc hydrothermal system. *Geochemistry International*, 50, No. 13, 1069–1100.
- 549 Hedin, L., and Lundqvist, B. (1971) Explicit local exchange-correlation potentials. *Journal*  
550 *of Physics C: Solid State Physics*, 4, 2064–2083.
- 551 Huheey, J.E., Keiter, E.A., and Keiter, R.L. (2000) *Inorganic chemistry. Principles of*  
552 *structure and reactivity*. 4<sup>th</sup> edition, Pearson Education.
- 553 Ivanova, Ju.N., Tykova, E.E., Abramova, V.D., Kovalchuk, E.V., and Vikentyev, I.V.  
554 (2015) Ores mineralogy and first data about “invisible” form of Au in pyrite of the Novogodnee-  
555 Monto deposit (the Polar Urals, Russia). In A.-S. André-Meyer et al., Eds., *Proceedings of the*  
556 *13<sup>th</sup> Biennial SGA Meeting, Mineral Resources in a Sustainable World*, p. 121-125. Nancy,  
557 France.
- 558 Joly, Y. (2001). X-ray absorption near-edge structure calculations beyond the muffin-tin  
559 approximation. *Physical Review B*, 63, 125120-125129.
- 560 Kozerenko, S.V., Wagner, F.E., Friedl, J., and Fadeev, V.V. (2001) Gold in pyrite  
561 formation processes: 3. Mössbauer study of synthetic gold-bearing iron sulfides. *Geochemistry*  
562 *International*, 39, Suppl. 2, S167-S172.
- 563 Kresse, G. (1999). From ultrasoft pseudopotentials to the projector augmented-wave  
564 method. *Physical Review B*, 59, 1758–1775.
- 565 Kuhn, M., and Sham, T.K. (1994) Charge redistribution and electronic behavior in a series  
566 of Au-Cu alloys. *Physical Review B*, 49, 1647-1661.
- 567 Kvashnina, K.O., and Scheinost, A.C. (2016) A Johann-type X-ray emission spectrometer  
568 at the Rossendorf Beamline. *Journal of Synchrotron Radiation*, 23, 836–841.
- 569 Laptev, Yu.V., and Rozov, K.B. (2006) Interaction of gold with sulfide surface as a factor  
570 of its concentration in hydrothermal ore formation. *Doklady Earth Sciences*, 411, No. 8, 1229-  
571 1232.



- 572 Large, R.R., Maslennikov, V.V., Robert, F., Danyushevsky, L.V., and Chang, Z. (2007)  
573 Multistage sedimentary and metamorphic origin of pyrite and gold in the giant Sukhoi Log  
574 deposit, Lena Gold Province, Russia. *Economic Geology*, 102, 1233-1267.
- 575 Lutz, H.D., Jung, M., and Wäschenbach, G. (1987) Kristallstrukturen des löllingits  $\text{FeAs}_2$   
576 und des pyrits  $\text{RuTe}_2$ . *Zeitschrift für Anorganische und Allgemeine Chemie*, 554, 87-91.
- 577 Mercier-Langevin, P., Hannington, M.D., Dubé, B., and Bécu, V. (2011) The gold content  
578 of volcanogenic massive sulfide deposits. *Mineralium Deposita*, 46, 509-539.
- 579 Otero-de-la-Roza, A., Blanco, M.A., Martín Pendás, A., and Luaña, V. (2009) Critic: a  
580 new program for the topological analysis of solid-state electron densities. *Computer Physics*  
581 *Communications*, 180, 157–166.
- 582 Otero-de-la-Roza, A., Johnson, E.R., and Luaña, V. (2014) Critic2: A program for real-  
583 space analysis of quantum chemical interactions in solids. *Computer Physics Communications*,  
584 185, 1007–1018.
- 585 Palenik, C.S., Utsunomiya, S., Reich, M., Kesler, S.E, Wang, L., and Ewing, R.C. (2004)  
586 “Invisible” gold revealed: Direct imaging of gold nanoparticles in a Carlin-type deposit.  
587 *American Mineralogist*, 89, 1359-1366.
- 588 Ravel, B., and Newville, M. (2005) ATHENA, ARTEMIS, HEPHAESTUS: data analysis  
589 for X-ray absorption spectroscopy using IFEFFIT. *Journal of Synchrotron Radiation*, 12, 537-  
590 541.
- 591 Rehr, J.J., Kas, J.J., Vila, F.D., Prange, M.P., and Jorissen, K. (2010). Parameter-free  
592 calculations of X-ray spectra with FEFF9. *Physical Chemistry Chemical Physics*, 12, 5503-5513.
- 593 Reich, M., Kesler, S., Utsunomiya, S., Palenik, C.S., Chryssoulis, S.L., and Ewing, R. C.  
594 (2005) Solubility of gold in arsenian pyrite. *Geochimica et Cosmochimica Acta*, 69, 2781-2796.

- 595 Reich, M., and Becker, U. (2006) First-principles calculations of the thermodynamic  
596 mixing properties of arsenic incorporation into pyrite and marcasite. *Chemical Geology*, 225,  
597 278–290.
- 598 Reich, M., Utsunomiya, S., Kesler, S., Wang, L., Ewing, R.C., and Becker, U. (2006)  
599 Thermal behavior of metal nanoparticles in geologic materials. *Geology*, 34, 1033-1036.
- 600 Renders, P.J., and Seward, T.M. (1989) The adsorption of thio gold(I) complexes by  
601 amorphous  $As_2S_3$  and  $Sb_2S_3$  at 25 and 90 °C. *Geochimica et Cosmochimica Acta*, 53, 255-267.
- 602 Savage, K.S., Tingle, T.N., O’Day, P.A., Waychunas, G.A., and Bird, D.K. (2000) Arsenic  
603 speciation in pyrite and secondary weathering phases, Mother Lode Gold District, Tuolumne  
604 County, California. *Applied Geochemistry*, 15, 1219-1244.
- 605 Simon, G., Huang, H., Penner-Hahn, J.E., Kesler, S., and Kao, L.S. (1999) Oxidation state  
606 of gold and arsenic in gold-bearing arsenian pyrite. *American Mineralogist*, 84, 1071-1079.
- 607 Stefánsson, A., and Seward, T.M. (2004) Gold(I) complexing in aqueous sulphide  
608 solutions to 500°C at 500 bar. *Geochimica et Cosmochimica Acta*, 68, 4121-4143.
- 609 Tagirov, B.R., Dikov, Yu.P., Buleev, M.I., Koval’chuk, E.V., Chareev, D.A., Kokh, M.A.,  
610 Borisovskii, S.E., Abramova, V.D., Baranova, N.N., Garas’ko, M.I., Kovalenker, V.A., and  
611 Bortnikov, N.S. (2014) “Invisible” gold in covellite (CuS): synthesis and studies by EPMA, LA–  
612 ICP–MS, and XPS techniques. *Doklady Earth Sciences*, 459, Part 1, 1381–1386.
- 613 Tagirov, B.R., Trigub, A.L., Kvashnina, K.O., Shiryaev, A.A., Chareev, D.A., Nickolsky,  
614 M.S., Abramova, V.D., and Kovalchuk, E.V. (2016) Covellite CuS as a matrix for “invisible”  
615 gold: X-ray spectroscopic study of the chemical state of Cu and Au in synthetic minerals.  
616 *Geochimica et Cosmochimica Acta*, 191, 58-69.
- 617 Vikentyev, I.V. (2015a) Invisible and microscopic gold in pyrite: methods and new data  
618 for massive sulfide ores of the Urals. *Geology of Ore Deposits*, 57, No. 4, 237-265.

- 619 Vikentyev, I.V. (2015b) Invisible and microscopic gold in pyrite: new data for  
620 volcanogenic massive sulfide ores of the Urals. In A.-S. André-Meyer et al., Eds., Proceedings of  
621 the 13<sup>th</sup> Biennial SGA Meeting, Mineral Resources in a Sustainable World, p. 2113-2116.  
622 Nancy, France.
- 623 Vikent'eva, O.V., and Bortnikov, N.S. (2015) The large Svetlinsk Au-Te deposit, South  
624 Urals: telluride mineralization for genetic reconstructions. In A.-S. André-Meyer et al., Eds.,  
625 Proceedings of the 13<sup>th</sup> Biennial SGA Meeting, Mineral Resources in a Sustainable World, p.  
626 851-854. Nancy, France.
- 627 Wagner, T., Klemm, R., Wenzel, T., and Mattson, B. (2007) Gold upgrading in  
628 metamorphosed massive sulfide ore deposits: Direct evidence from laser-ablation-inductively-  
629 coupled plasma mass spectrometry of invisible gold. *Geology*, 35, 775-778.
- 630 Watson, R.E., Hudis, J., and Perlman, M.L. (1971) Charge flow and *d* compensation in  
631 gold alloys. *Physical Review B*, 4, 4139-4144.
- 632 Widler, A.M., and Seward, T.M. (2002) The adsorption of gold (I) hydrosulphide  
633 complexes by iron sulphide surfaces. *Geochimica et Cosmochimica Acta*, 66, 383-402.
- 634 Zabinsky, S.I., Rehr, J.J., Ankudinov, A., Albers, R.C., and Eller, M.J. (1995) Multiple-  
635 scattering calculations of X-ray-absorption spectra. *Physical Review B*, 52, 2995-3009.
- 636 Zotov, A.V., Laputina, I.P., and Chichagov, A.V. (1972) Arsenian pyrite from hot springs  
637 of Kunashir Island (Kuril Islands). *Geology of Ore Deposits*, No. 1, 125-131 (in Russian).  
638

639  
640

**Table 1.** Position of edge jump (e.j.) and white line (WL) of Au L<sub>3</sub> edge HERFD-XANES spectra. Uncertainty is ± 0.2 eV.

Sample/Standard	Feature	Position, eV
Löllingite FeAs <sub>2</sub>	e.j. WL	11920.1 11922.0
Arsenopyrite FeAsS	e.j. WL	11919.7 11921.5
Hydrothermal pyrite FeS <sub>2</sub>	e.j. WL	11918.6 11920.3
AuSb <sub>2</sub>	e.j. WL	11919.4 11920.0
Au <sub>2</sub> Bi	e.j. WL	11918.6 11921.2
Au <sub>2</sub> S	e.j. WL	11919.0 11921.3
Au metal	e.j. WL	11918.1 11921.1

641  
642  
643  
644  
645  
646

**Table 2.** Au local atomic structure in pyrite and löllingite determined by EXAFS fitting and DFT calculations. The last column shows interatomic distances for the unrelaxed structure of pure minerals. Uncertainties are calculated by the Artemis code.

Bond	EXAFS					Quantum Espresso <i>R</i> , Å	Crystal structure <sup>1</sup>
	<i>N</i>	<i>R</i> , Å	$\sigma^2$ , Å <sup>-2</sup>	<i>E</i> <sup>0</sup> , eV	Fit quality, R-factor		
Au in pyrite							
Au-S	6	2.40±0.028	0.014±0.0014			2.455	2.264
Au-S	6	3.51±0.16	0.027±0.024	6.4± 3.5	0.005	3.499	3.445
Au-S	2	3.69±0.11	0.008±0.018			3.854	3.613
Au-Fe	12	3.79±0.19	0.034±0.023			3.577	3.830
Au in löllingite							
Au-As	6	2.52±0.007	0.005±0.00003			2.536	2.361
Au-Fe	2	3.00±0.025	0.006±0.002			2.973	2.882
Au-As	4	3.88±0.032	0.006±0.004			3.739	3.726
Au-As	6	4.06±0.056	0.006±0.004	1.2± 1.9	0.011	3.984	3.927
Au-Fe	8	4.23±0.032	0.008±0.007			4.261	4.249
Au-As	4	4.67±0.054	0.004±0.010			4.737	4.723
Au-As	6	4.82±0.058	0.004±0.010			4.869	4.871
<sup>1</sup> unrelaxed structures: Bayliss (1977) for pyrite and Lutz et al. (1987) for löllingite.							

647

648 **Table 3.** Au local atomic structure in arsenopyrite determined by DFT  
 649 calculations compared to the unrelaxed structure of pure arsenopyrite.  
 650

Bond	<i>N</i>	Quantum Espresso <i>R</i> , Å	Crystal structure <sup>1</sup> <i>R</i> , Å
Au-S	3	2.466	2.231
Au-As	3	2.530	2.397
Au-Fe	2	2.984;3.655	2.734;3.741
Au-S	4	3.719;3.739;3.779; 3.781	3.681;3.725;3.762;3.762
Au-As	4	3.791;3.811;3.913;3.919	3.693;3.3.755;3.755;3.798

<sup>1</sup> unrelaxed structure from Bindi et al. (2012).

651  
 652 **Table 4.** Calculated Bader atomic partial charges for pure  
 653 and Au-bearing pyrite, löllingite, arsenopyrite, and for  
 654 Au<sub>2</sub>S<sub>(cr)</sub>. Literature data (Tagirov et al., 2016) on charges  
 655 of atoms in covellite CuS are given for comparison.  
 656

Au	Fe	As	S
FeAs <sub>2</sub>			
	+0.16	-0.08	
FeAsS			
	+0.42	+0.18	-0.6
FeS <sub>2</sub>			
	+0.70		-0.35
Au in FeAs <sub>2</sub> (nearest atoms to Au)			
-0.37	+0.18	-0.08; -0.01	
Au in FeAsS (nearest atoms to Au)			
-0.01	+0.43	+0.30	-0.56
Au in FeS <sub>2</sub> (nearest atoms to Au)			
+0.42	+0.72		-0.36
Au in Au <sub>2</sub> S <sup>1</sup>			
+0.21			-0.42
Au	Cu	S	
CuS			
	+0.56, +0.50	-0.84, -0.82(S <sub>2</sub> )	
Au in CuS (nearest atoms to Au)			
+0.19	+0.56, +0.48	-0.69, -0.80(S <sub>2</sub> )	

<sup>1</sup> calculated for the Au<sub>2</sub>S structure relaxed by DFT method, optimized lattice constant *a* = 5.35 Å, Au-S distance *R* = 2.32 Å.

657

## Figure Captions

**Figure 1.** Results of the pyrite hydrothermal synthesis experiment,  $t = 450\text{ }^{\circ}\text{C}$ ,  $P = 1\text{ kbar}$ . **A** - BSE image of the fine-grained aggregate of the synthetic pyrite; **b** - the concentration of Au in pyrite and coexisting aqueous fluid as a function of sulfur fugacity. Filled symbols – sulfur was used to control  $f(\text{S}_2)$ ; empty symbols correspond to the  $\text{S} + \text{H}_2\text{SO}_4$  system (last row in Table S1), where  $f(\text{S}_2)$  value has to be corrected.

**Figure 2.** Difference between the TFY and HERFD spectra for the löllingite sample,  $C(\text{Au}) = 800\text{ ppm}$ . In TFY mode, the Au features are completely masked by the As K edge. The HERFD mode makes it possible to record the Au  $L_3$  edge spectra.

**Figure 3.** The Au  $L_3$  edge HERFD-XANES spectra of the Au-bearing pyrite (hydrothermal synthesis, sample 6-16), arsenopyrite, löllingite (salt flux synthesis), and model substances. **A** - comparison with  $\text{Au}_{(\text{cr})}$  and  $\text{Au}_2\text{S}_{(\text{cr})}$ ; **b** - enlarged energy scale, a comparison of arsenopyrite and löllingite with  $\text{AuSb}_2$  and  $\text{Au}_2\text{Bi}$ . Note that the spectra of all the samples of hydrothermal pyrites shown in Fig. 1 were similar to the spectra of sample 6-16 shown in this figure.

**Figure 4.** The Au  $L_3$  edge HERFD-XANES spectra of pyrites synthesized using the hydrothermal (sample 6-16,  $C(\text{Au}) = 36\text{ ppm}$ ) and salt flux techniques (CD-624,  $C(\text{Au}) \sim 60\text{ ppm}$ , measured concentrations of Au in this sample are listed in Table S2). The heating of hydrothermal pyrite resulted in a decomposition of the chemically bound Au and a decrease in signal intensity. At  $630\text{ }^{\circ}\text{C}$ , the spectra corresponded to the traces of the chemically bound Au whose concentration continuously decreased with time during the experiment (see text for explanation). Vertical lines indicate the position of the 3 main features of  $\text{Au}_{(\text{cr})}$ .

**Figure 5.** EXAFS spectra of Au-bearing pyrite (*left pannel*, hydrothermal synthesis) and löllingite (*right pannel*, salt flux synthesis). *Top* – background subtracted EXAFS spectra,  $k^2$  weighted; *bottom* – Fourier transforms of the  $k^2$  weighted EXAFS spectra, not corrected for phase shift. Paths are indicated near the FT features. Thin black lines – experiment, thick red lines – fit results.

**Figure 6.** Results of a theoretical calculation of Au  $L_3$  edge HERFD-XANES spectra for Au-bearing pyrite (**a**), löllingite (**b**), and arsenopyrite (**c**). Experimental spectra are shown for comparison (*Pyrite*: sample 6-16, hydrothermal,  $C(\text{Au}) = 36\text{ ppm}$ ; *Löllingite*: sample 5333, salt flux synthesis,  $C(\text{Au}) = 800 \pm 300\text{ ppm}$ ; *Arsenopyrite*: sample 5140, salt flux synthesis,  $C(\text{Au}) = 23 \pm 14\text{ ppm}$ ). For pyrite, the EXAFS structure was built by setting the first-neighbour Au-S distances in accordance with the EXAFS model (Table 2), whereas all the other distances were adopted from the unrelaxed structure of pure pyrite.

a

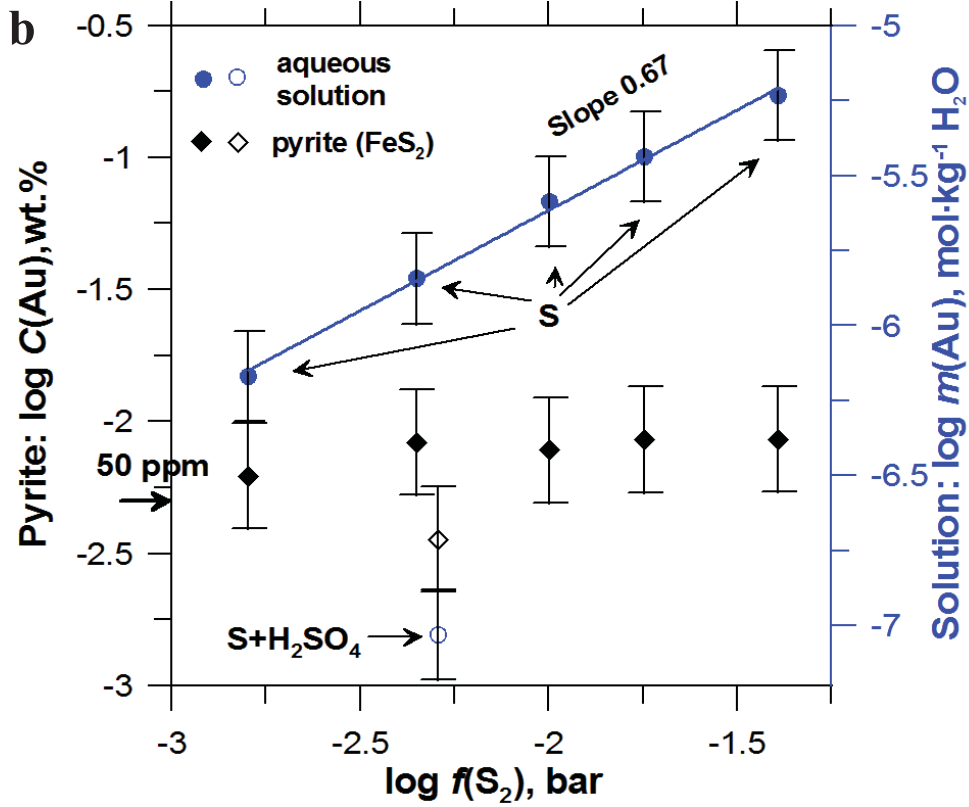
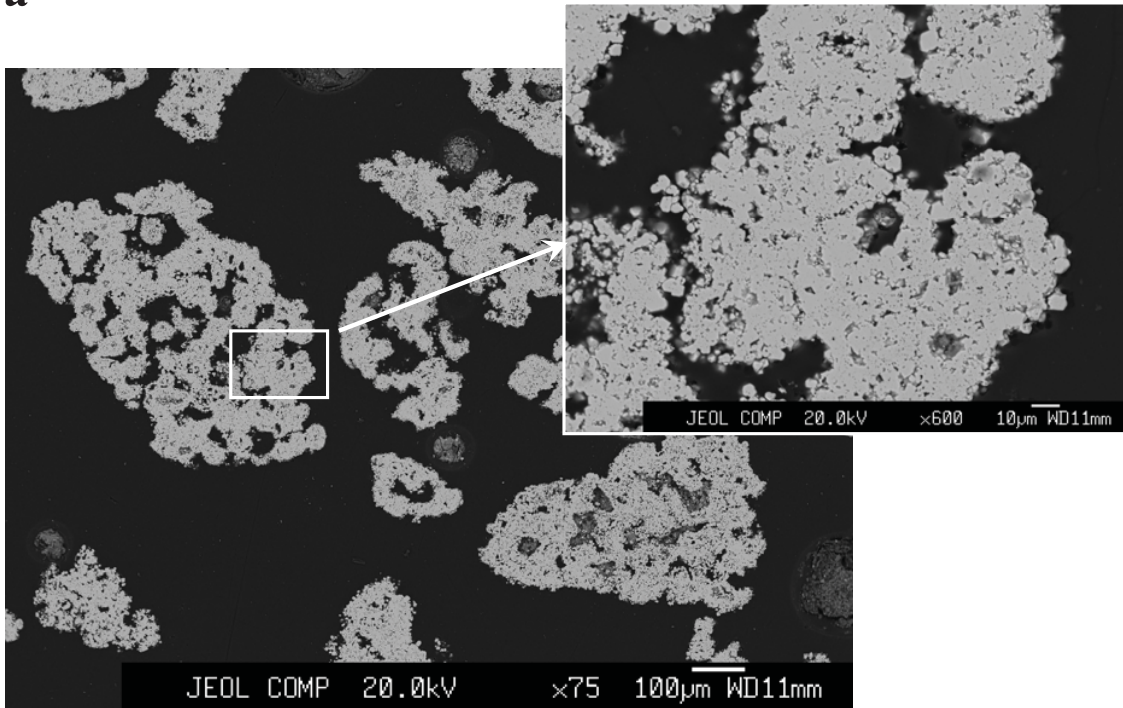


Fig. 1.

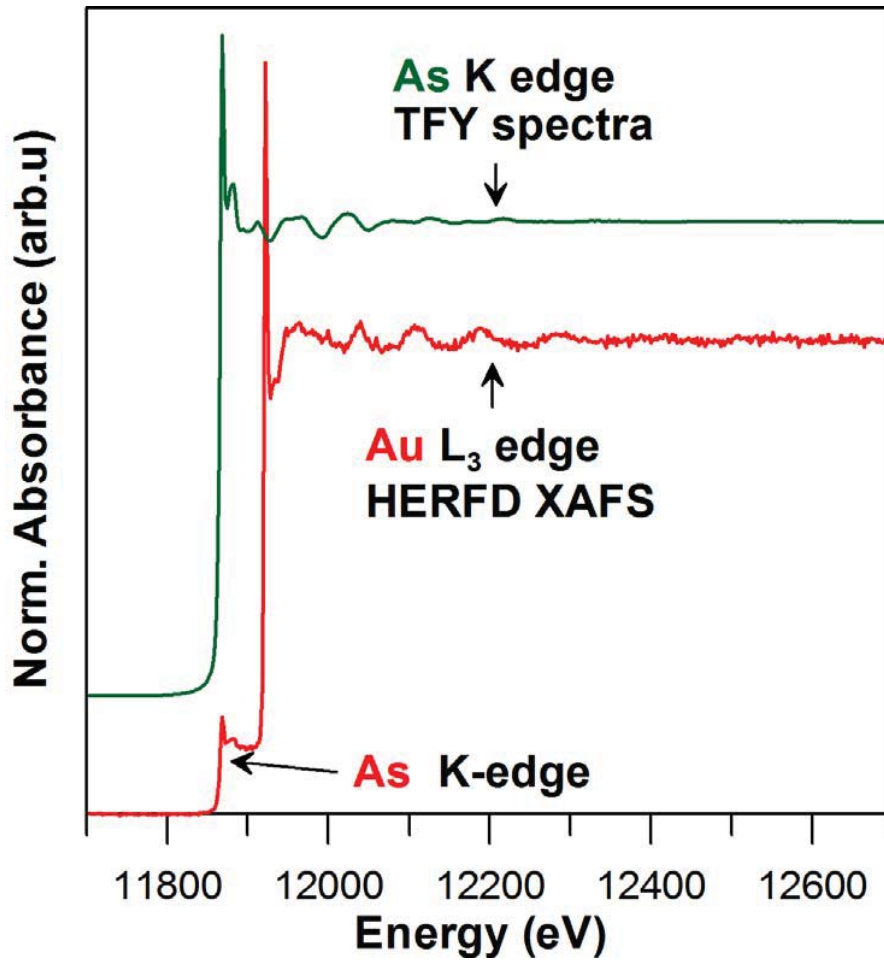


Fig. 2.



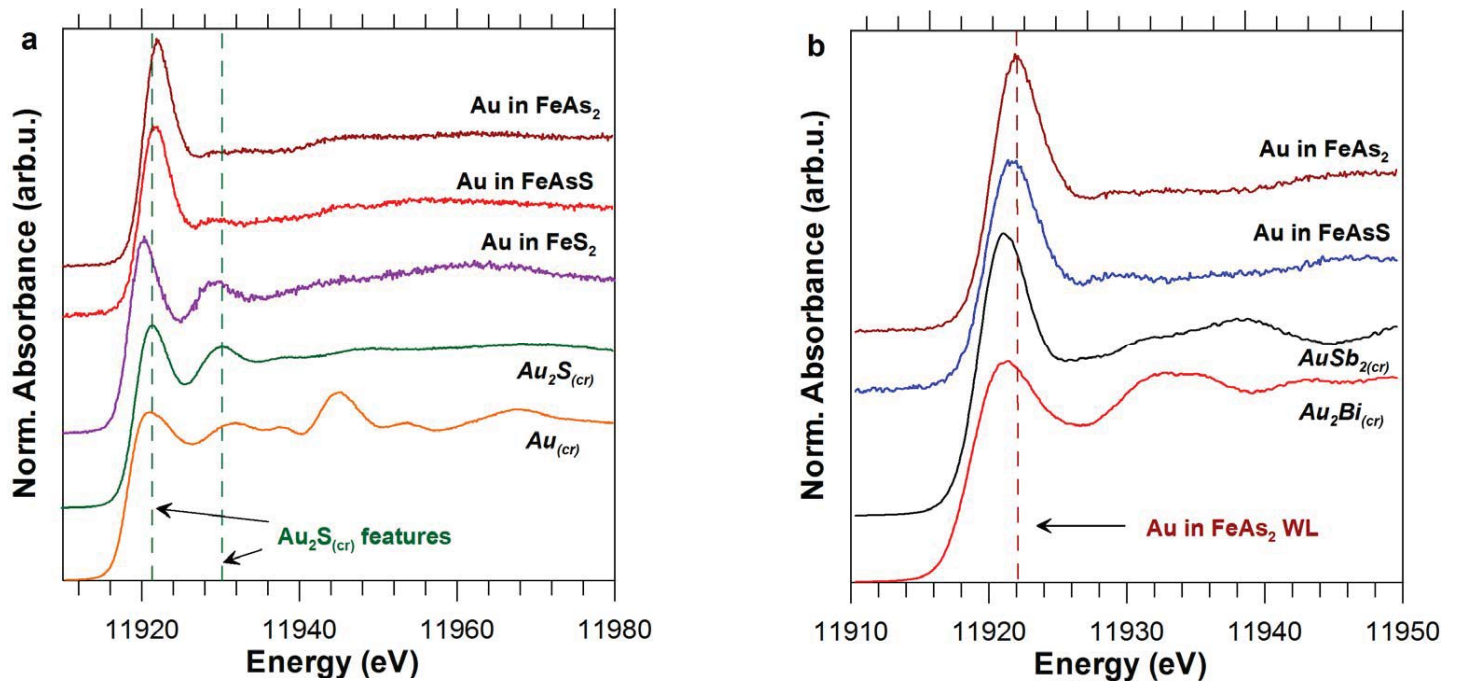


Fig. 3.

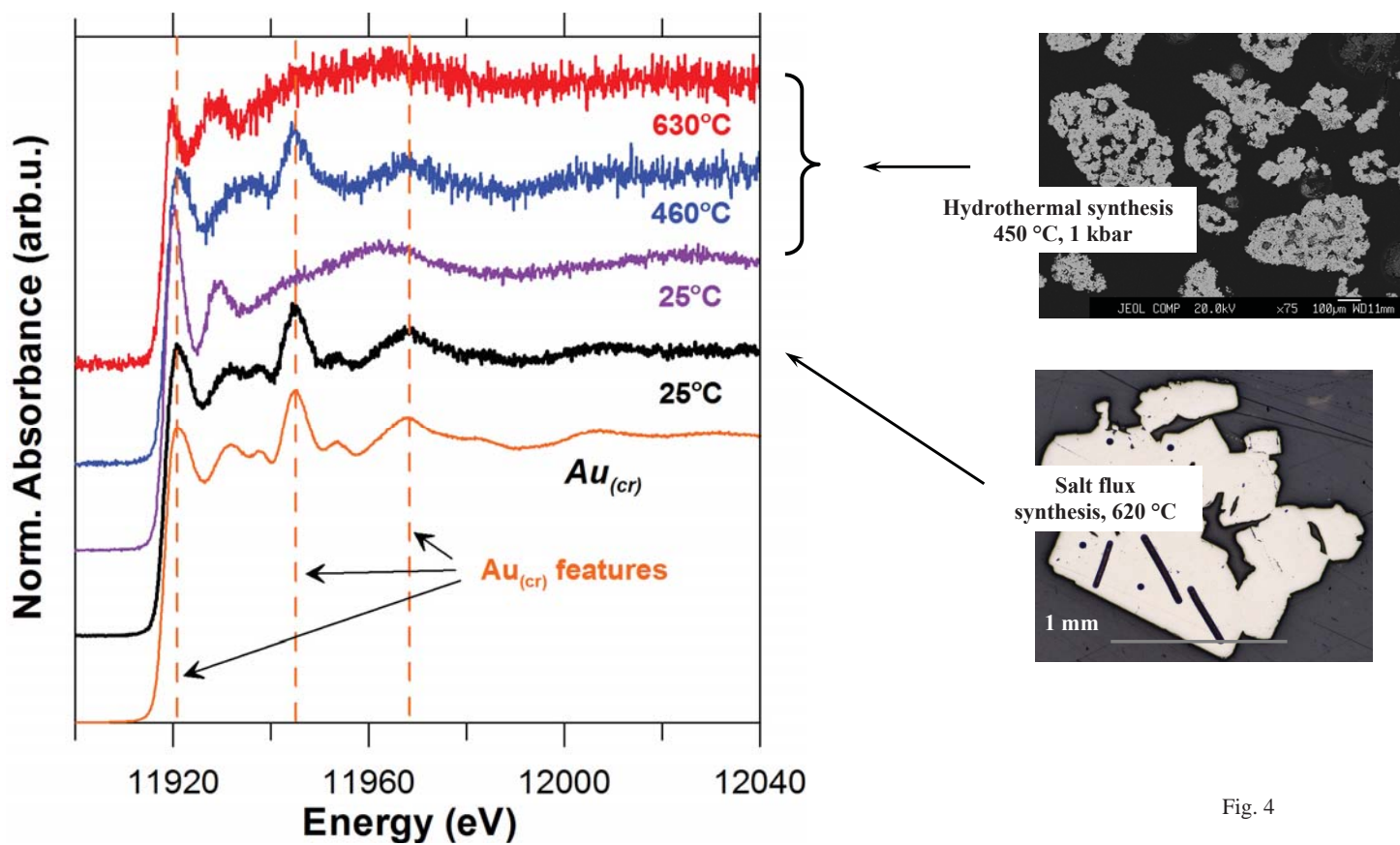


Fig. 4

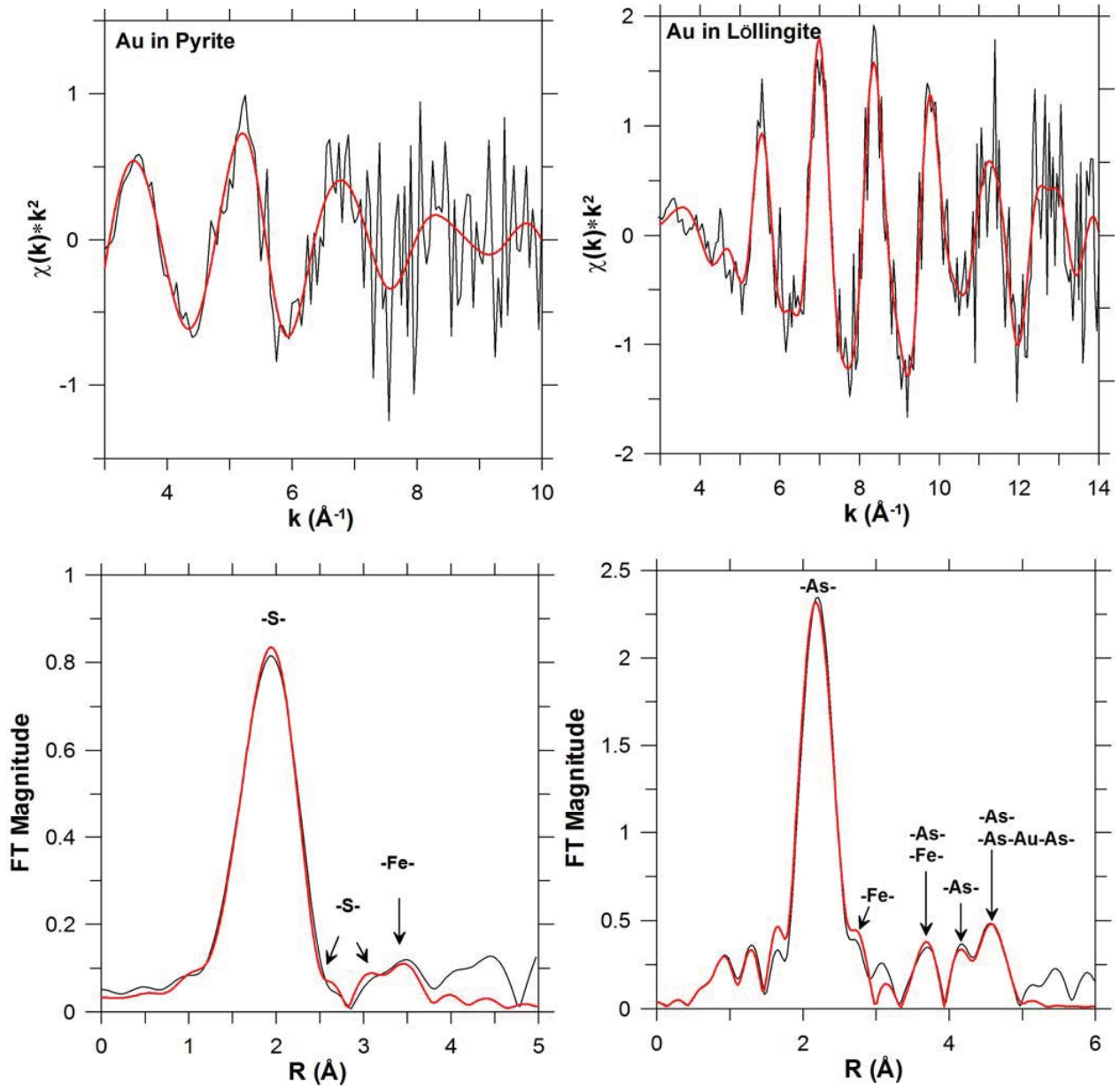


Fig. 5

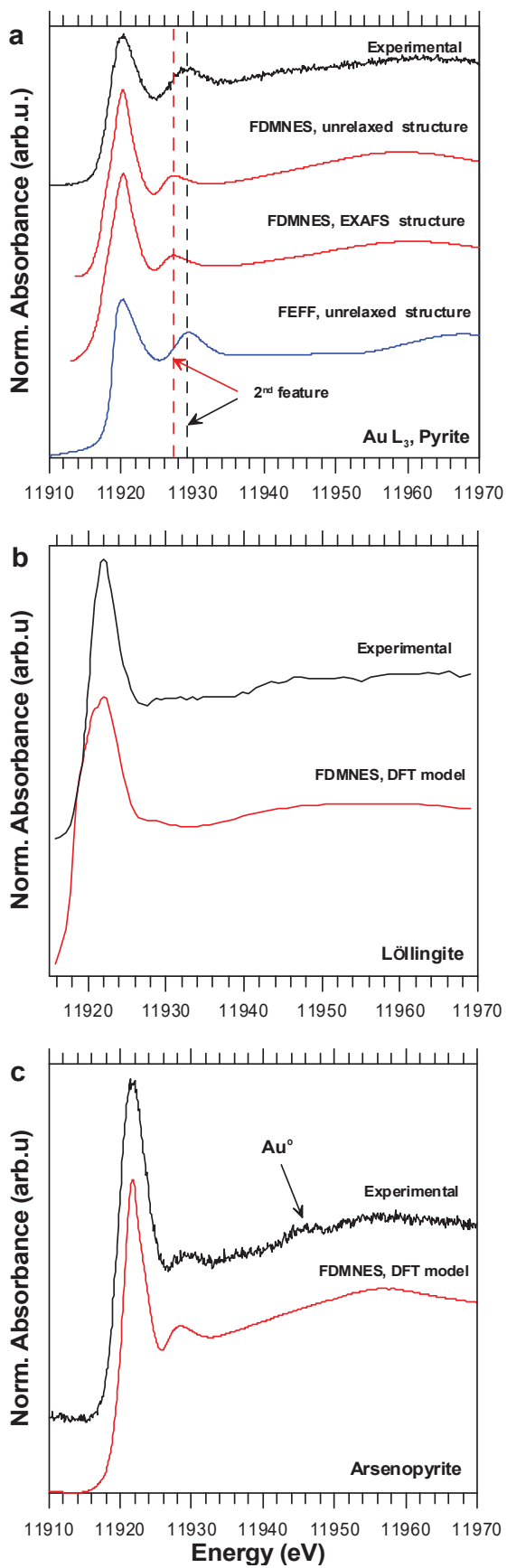


Fig. 6